Synchronous Switching of Non-Line-Start Permanent Magnet Synchronous Machines From Inverter to Grid Drives

Ronggang Ni, *Student Member, IEEE*, Dianguo Xu, *Senior Member, IEEE*, Gaolin Wang, *Member, IEEE*, Guoqiang Zhang, and Chengrui Li

***Abstract*—Non-line-start permanent magnet synchronous machines (NLSPMSMs) are normally considered not able to operate stably under grid drive. However, this paper proposes an effective control strategy to achieve soft start and synchronous switching of NLSPMSMs from inverter to grid drives so that to extend the application field. The system electromechanical model during switching is deduced and analyzed numerically to verify the stability under grid drive. For the control strategy, model-based sliding-mode observer is adopted during soft start for low-cost position sensorless drive, and two digital phase lock loops are used to obtain the phases of grid and inverter voltages for phase tracking. Experiments are carried out on five NLSPMSMs with different rated powers and velocities, and test results show that all these prototypes can be safely switched to grid drive and robust to load variation. Tested waveforms are coincident with numerical analysis, and the system efficiencies of NLSPMSMs under inverter and grid drives are compared.**

***Index Terms*—Nonline-start permanent magnet synchronous machine (NLSPMSM), system stability, soft start, synchronous switching.**

NOMENCLATURE

ω_m	Electric rotating velocity of NLSPMSM.
ω_g	Electric rotating velocity of grid, in this paper, $\omega_g = 100\pi\ \mathrm{rad/s}$.
θ	Torque angle between grid voltage and rotational q-axis of NLSPMSM.
θ_g	Initial torque angle under inverter drive.
θ_0	Initial torque angle at the time of switching to grid drive.
ω_{m0}	Initial electric rotating velocity of NLSPMSM at the time of switching to grid drive.
p	Number of pole pairs of NLSPMSM.
$L_{d,q}$	D- and q-axis inductances of NLSPMSM.
R_1	Phase winding resistance of NLSPMSM.
ψ_f	Permanent magnet flux linkage of NLSPMSM.
J	Mechanical inertia.
k_D	Damping coefficient of friction resistance.
t_f	Switching dead time between two contactors.
$\vec{u}_{\mathrm{grid}}$	Synthetic vector of grid phase voltages.
U_{grid}	$\sqrt{3/2}$ times of the magnitude of $\vec{u}_{\mathrm{grid}}$.
$u_{g\alpha,g\beta}$	Clarke components of grid line voltages.
$u_{m\alpha,m\beta}$	Clarke components of inverter line voltages.
θ_{gv}	Grid voltage phase obtained from phase-locked loop (PLL).
θ_{mv}	Inverter voltage phase obtained from PLL.
*	Superscript ending with * indicates reference value for control.
R, *S*, *T*	Subscript ending with *R*, *S* or *T* indicates grid parameters.
U, *V*, *W*	Subscript ending with *U*, *V* or *W* indicates inverter parameters.

Manuscript received April 9, 2015; revised July 9, 2015; accepted July 18, 2015. Date of publication July 21, 2015; date of current version December 10, 2015. Recommended for publication by Associate Editor J. R. Espinoza.

The authors are with the School of Electrical Engineering and Automation, Harbin Institute of Technology, Harbin 150001, China (e-mail: ronni@hit.edu.cn; xudiang@hit.edu.cn; wg1818@hit.edu.cn; wisdom9527@163.com; angusrainrui@163.com).

Color versions of one or more of the figures in this paper are available online at http://ieeexplore.ieee.org.

Digital Object Identifier 10.1109/TPEL.2015.2459595

I. INTRODUCTION

PERMANENT magnet synchronous machines (PMSMs) have been widely used because of high efficiency, high power factor, and excellent dynamic performance [1]. Traditionally, line-start PMSMs (LSPMSMs) with short-circuited rotor rings or damping windings can start online and be directly driven by grid [2]–[6]. However, they usually suffer from large start current and poor dynamic performance caused by asynchronous torque, and the negative torque generated by permanent magnets lowers the starting and synchronization capabilities during transient state [7], [8]. Besides, the large start current and asynchronous velocity during direct online start may cause demagnetization of permanent magnets [9]. Many researchers have attempted to overcome these disadvantages of LSPMSMs. However, simultaneously achieving high start torque, good synchronization capability, and excellent steady-state characteristics still remains unsolved and compromises are inevitable during optimization [10], [11]. Because of these drawbacks, LSPMSMs are receiving less attention, and hence induction machines (IMs), despite of their low efficiency, defeat PMSMs in constant speed drives.

PMSMs without damping windings, or non-line-start PMSMs (NLSPMSMs) are capable of excellent dynamic performance and super premium efficiency. However, they cannot start online because of no asynchronous torque, and may lose out of step without proper control. Therefore, they are mostly operated by inverters [12]. To improve the efficiency of constant speed drives and extend the application fields of NLSPMSMs, this paper investigates the system stability numerically and proposes an

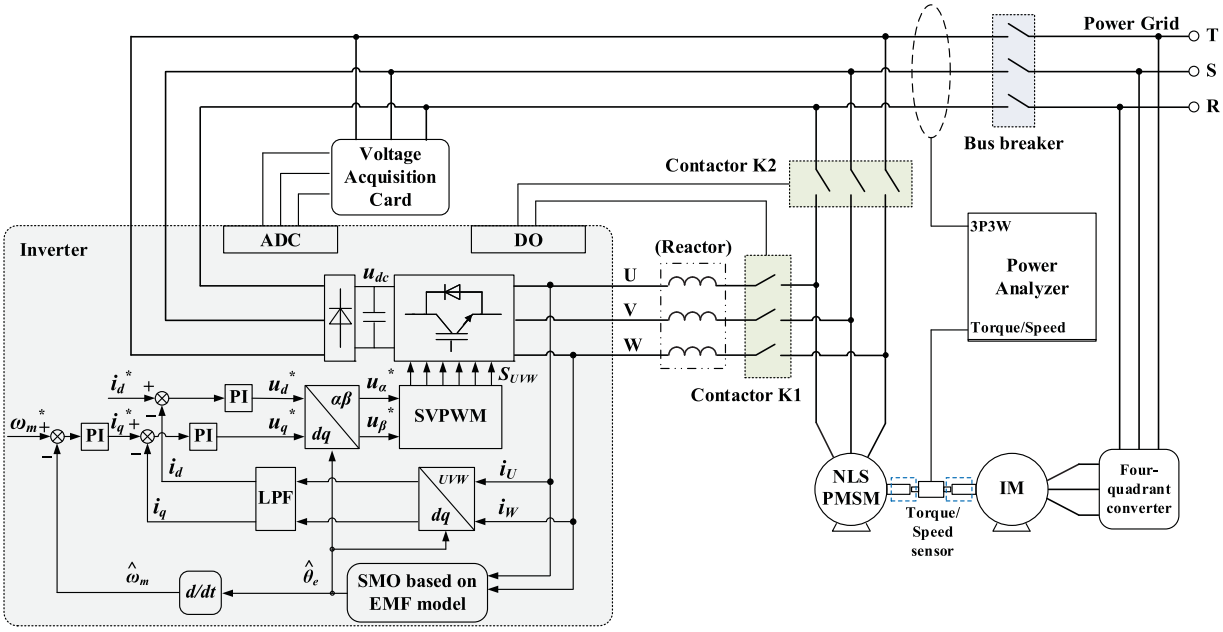

Fig. 1. System configuration for soft start and synchronous switching of NLSPMSM.

effective control strategy to operate NLSPMSMs from inverter to grid drives.

Because NLSPMSMs cannot start online, inverter-aided soft start is necessary. Even for IMs or LSPMSMs, soft start is preferred because direct online start results in severe transients in the machine and associated power system, which cannot be prevented by correct protection settings. Especially to prevent stator end-winding failure caused by the force proportional to the square of phase current, decreasing the starting current is the sole solution. To meet the increasing demand of less shock to the grid and less damage to the machine, soft start has been widely adopted in IMs and LSPMSMs. Soft start is often defined as a technology that provides adjustable voltage to the machine either by mechanical or power electronic devices [13]. Common methods for soft start are using Korndorfer-reduced voltage autotransformer or using autotransformer with capacitor assist [14]–[16], power electronic-aided reducing voltage starters [17], star-delta soft start [18], [19], adjustable voltage and frequency starting methods [20]–[26], etc. With the development of power electronics and advanced control strategies, inverter-aided soft start has become widely accepted because of high dynamic performance and small start current.

In this paper, the methodology of soft start and synchronous switching of NLSPMSMs is proposed and NLSPMSMs are first reported to operate stably under grid drive. The system configuration is first presented in Section II. Then, the system electromechanical model is built and solved numerically to discuss the system stability during switching. Later in Section V, a control strategy including both position sensorless soft start and PLL-aided phase tracking are proposed. Finally, five NLSPMSM prototypes with different rated powers and velocities are successfully switched to grid drive, and the efficiencies of NLSPMSM systems under grid drive are tested to be higher than those of inverter especially at high loads, hence, more efficient control strategy of NLSPMSMs can be designed.

II. System Configuration

The system configuration for soft start and synchronous switching of NLSPMSMs is shown in Fig. 1. During soft start, contactor K2 is open and K1 is closed so that NLSPMSM is driven by inverter. To reduce the system cost, mechanical position sensor is eliminated and hybrid sensorless control, especially the electromotive force (EMF) model-based sliding-mode observer (SMO) is used to estimate the rotor position and velocity at medium and high speed [27], [28]. The magnitude of inverter output voltage is adjusted by d-axis current reference i_d^*, and the frequency and phase are regulated by the velocity reference ω_m^*. The detailed control strategy for switching will be discussed in Section V.

Grid voltage information is obtained from the voltage acquisition card and processed via analog-to-digital converter for switching control. When the inverter and grid voltages share close magnitude, frequency, and phase, two switching signals are exerted through digital output to first turn off contactor K1 and then turn on contactor K2. Several milliseconds of switching dead time are essential to avoid current flowing back from grid to inverter. Normally, the contactor turn-on time is longer than turn-off time, and hence the two switching signals can be generated simultaneously. A reactor or isolation transformer between contactor K1 and inverter is optional in case the switching dead time is so short that the inverter is short-circuited. In this paper, the switching dead time is long enough, and hence the reactor is not necessary. As the NLSPMSM is out of inverter control during grid drive, a bus breaker with proper capacity is necessary for overcurrent protection. Note that the inverter

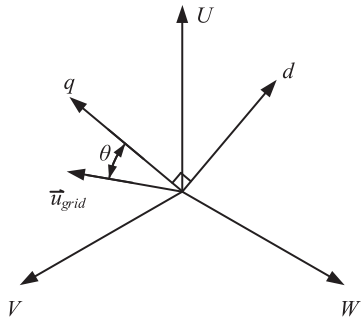

Fig. 2. Vector diagram of grid voltage in rotational *d–q* axis of NLSPMSM.

output voltages should be in the same sequence as those of the grid to drive the NLSPMSM in the same direction.

In this paper, an IM driven by a four-quadrant converter is used for load. The NLSPMSM system efficiency is tested from a power analyzer by measuring the grid input electric power and mechanical output power so that the inverter loss is also considered.

III. Electromechanical Model During Switching

The system electromechanical model during switching consists of three parts, i.e., grid voltages, NLSPMSM voltages, and mechanical coupling. The respective models are deduced in this section, from which the state equation during switching from inverter drive to grid drive is obtained.

A. Grid Model in Voltage Equations

The vector diagram of grid voltage is drawn in rotational *d–q* axis as shown in Fig. 2, where

$$\vec{u}_{\rm grid} = \frac{2}{3}\left(u_R + u_S e^{j\frac{2\pi}{3}} + u_T e^{j\frac{4\pi}{3}}\right) \tag{1}$$

is the synthetic grid voltage vector. u_R, u_S, and u_T are the grid three-phase voltages in instantaneous values

$$\begin{cases} u_R = 311\cos\left(2\pi\cdot 50\cdot t\right) \\ u_S = 311\cos\left(2\pi\cdot 50\cdot t - 2\pi/3\right) \\ u_T = 311\cos\left(2\pi\cdot 50\cdot t - 4\pi/3\right) \end{cases} \tag{2}$$

where 311 V is the magnitude of grid phase voltages in this paper, and 50 Hz is the typical frequency.

The phase angle between $\vec{u}_{\rm grid}$ and rotor q-axis is defined as θ, which is known as the torque angle. After switching to grid drive, θ satisfies

$$\theta = \int_0^t (\omega_g - \omega_m)dt + \theta_0 \tag{3}$$

where θ_0 is the initial torque angle when contactor K2 is closed, i.e., $t = 0$. ω_g and ω_m are the electric rotating velocities of grid and inverter voltage vectors, and $\omega_g = 100\pi$ rad/s

$$\omega_m = 2\pi\frac{np}{60} \tag{4}$$

where n is the mechanical velocity of NLSPMSM in r/min value, and p is the pole pairs.

By decoupling $\vec{u}_{\rm grid}$ into rotational d- and q-axis voltages of NLSPMSM as referred to Fig. 2, we have

$$\begin{cases} u_d = -U_{\rm grid}\sin\theta \\ u_q = U_{\rm grid}\cos\theta \end{cases} \tag{5}$$

where $U_{\rm grid}$ is defined as $\sqrt{3/2}$ times of the magnitude of $\vec{u}_{\rm grid}$, $U_{\rm grid} \approx 380\,\text{V}$. After switching to grid drive, the machine is driven by the voltages in (5). Before that, u_d and u_q are both zero because of the switching dead time between two contactors.

B. PMSM Model in Voltage Equations

The NLSPMSM model in voltage equations is

$$\begin{cases} u_d = L_d\dfrac{di_d}{dt} + R_1 i_d - \omega_m L_q i_q \\ u_q = L_q\dfrac{di_q}{dt} + R_1 i_q + \omega_m L_d i_d + \omega_m \psi_f \end{cases} \tag{6}$$

where L_d and L_q are the d- and q-axis inductances and R_1 is the stator resistance. ψ_f is the PM flux linkage.

After switching to grid drive, i.e., $t \geq 0$, u_d and u_q in (5) and (6) are equivalent. Therefore, the electric system equations under grid drive are derived as

$$\begin{cases} -U_{\rm grid}\sin\theta = L_d\dfrac{di_d}{dt} + R_1 i_d - \omega_m L_q i_q \\ U_{\rm grid}\cos\theta = L_q\dfrac{di_q}{dt} + R_1 i_q + \omega_m L_d i_d + \omega_m \psi_f . \end{cases} \tag{7}$$

C. PMSM Mechanical Model

The general mechanical equation is

$$J\frac{d\left(\omega_m/p\right)}{dt} = T_{\rm em} - T_L - T_D \tag{8}$$

where J is the system inertia, T_{em} is the electromagnetic torque of NLSPMSM

$$T_{\rm em} = p\left[\psi_f i_q + \left(L_d - L_q\right) i_d i_q\right]. \tag{9}$$

T_L is load torque and T_D is the friction resistance torque proportional to rotating velocity

$$T_D = k_D\omega_m \tag{10}$$

where k_D is the damping coefficient of friction resistance.

Therefore, the mechanical model of NLSPMSM is

$$\frac{d\omega_m}{dt} = \frac{p^2}{J}\left[\psi_f i_q + \left(L_d - L_q\right) i_d i_q\right] - \frac{p}{J}T_L - \frac{p}{J}k_D\omega_m . \tag{11}$$

D. System Electromechanical Model

Combining (3), (7), and (11), we can derive the system state equations of NLSPMSM after switching to grid drive as (12). Obviously, the deduced equations are highly nonlinear, and need to be solved numerically. Before that, the initial values of state

variables should be known

$$\begin{cases} \dot{i}_d = \dfrac{1}{L_d}\left(-U_{\text{grid}}\sin\theta - R_1 i_d + \omega_m L_q i_q\right) \\ \dot{i}_q = \dfrac{1}{L_q}\left(U_{\text{grid}}\cos\theta - R_1 i_q - \omega_m L_d i_d - \omega_m \psi_f\right) \\ \dot{\omega}_m = \dfrac{p^2}{J}\left[\psi_f i_q + \left(L_d - L_q\right) i_d i_q\right] - \dfrac{p}{J}T_L - \dfrac{p}{J}k_D\omega_m \\ \dot{\theta} = \omega_g - \omega_m . \end{cases} \tag{12}$$

E. Initial Values of State Variables

The initial values of state variables are needed to solve (12). To avoid current flowing back from grid to inverter, there is adequate switching dead time between contactor K1 and K2, during which the NLSPMSM is stopping freely. Therefore, when contactor K2 is closed, there is no current in windings and hence

$$i_{d0} = i_{q0} = 0. \tag{13}$$

The initial value of ω_m and θ is dependent on the switching dead time for free stop. According to (3) and (11), the mechanical state equations during free stop is

$$\begin{cases} \dfrac{d\omega_m}{dt} = -\dfrac{p}{J}T_L - \dfrac{p}{J}k_D\omega_m \\ \dfrac{d\theta}{dt} = \omega_g - \omega_m . \end{cases} \tag{14}$$

The initial values of ω_m for (14) at the time when contactor K1 is open should be the same as grid voltage vector velocity ω_g, which is one of the major tasks for switching control. And the initial value of θ for (14) is assumed as θ_g which is the torque angle for stable operation under inverter drive. Before switching, the inverter voltage vector is controlled in the same phase as grid. Therefore, θ_g is also the angle between grid voltage and rotational q-axis. Therefore, the Laplace transformation of the first equation in (14) is

$$\frac{J}{p}\left(s\Omega_m - \omega_g\right) = -\frac{T_L}{s} - k_D\Omega_m \tag{15}$$

and hence

$$\Omega_m = \frac{\omega_g + \frac{T_L}{k_D}}{s + \frac{p}{J}k_D} - \frac{\frac{T_L}{k_D}}{s}. \tag{16}$$

Adopting inverse Laplace transformation, ω_m during free stop is solved as

$$\omega_m = \left(\omega_g + \frac{T_L}{k_D}\right)e^{-\frac{p}{J}k_D t_f} - \frac{T_L}{k_D}. \tag{17}$$

After free stop time t_f, the inverter voltage electric velocity at the time when contactor K2 is closed is obtained as

$$\omega_{m0} = \left(\omega_g + \frac{T_L}{k_D}\right)e^{-\frac{p}{J}k_D t_f} - \frac{T_L}{k_D}. \tag{18}$$

TABLE I
PARAMETERS OF NLSPMSM PROTOTYPES

Parameters of NLSPMSM prototypes					
Rated power (kW)	2.2	5.5	7.5	15	37
Rated frequency (Hz)	50				
Rated current (A)	4.5	10	13	25	61
Winding Connection	Wye	Delta			
p	3	2	1	3	3
L_d (mH)	32	55	70	21	10
L_q (mH)	62	159	232	58	49
R_1 (Ω)	2.6	2.3	1.9	0.6	0.3
ψ_f (Wb)	1.014	1.853	1.781	1.858	1.985
J (kg·m^2)	0.15	1.00	0.99	1.17	1.60
k_D (N·m·s/rad)	0.001	0.006	0.005	0.011	0.029
t_f (ms)	20	20	20	30	30

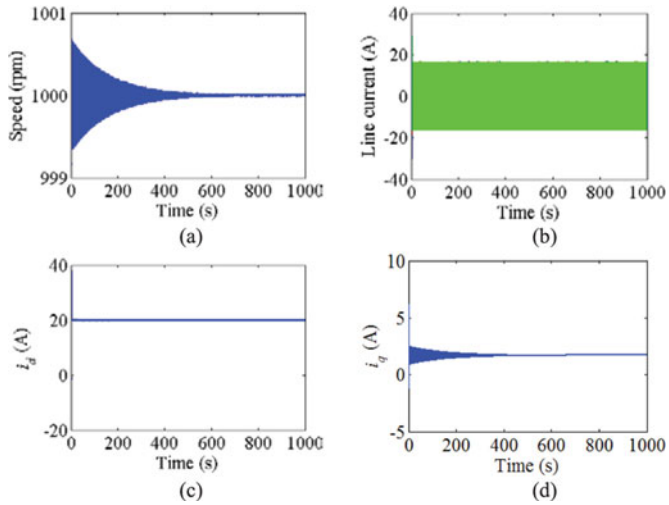

Fig. 3. Numerical calculation after switching to grid drive based on the 37 kW NLSPMSM with parameters listed in Table I. (a) Calculated mechanical velocity. (b) Calculated line currents. (c) Calculated d-axis current. (d) Calculated q-axis current.

The torque angle between grid voltage and rotor q-axis when contactor K2 is closed can be obtained from integration

$$\begin{aligned} \theta_0 &= \theta_g + \int_0^{t_f}\left(\omega_g - \omega_m\right)dt \\ &= \theta_g + \left(\omega_g + \frac{T_L}{k_D}\right)\left(t_f + \frac{e^{-\frac{p}{J}k_D t_f} - 1}{\frac{p}{J}k_D}\right) \end{aligned} \tag{19}$$

where ω_m satisfies (17).

IV. NUMERICAL ANALYSIS OF SYSTEM STABILITY

The deduced nonlinear state equations are solved numerically using fourth- and fifth-order Runge–Kutta algorithm on a 37 kW NLSPMSM prototype with parameters listed in Table I. The calculated results are shown in Fig. 3. It can be seen the mechanical speed is convergent, and the system is stable after switching to grid drive. The switching dead time not only causes delays in motor speed and phase, but also clears the armature current. When grid voltage is applied, a transient process is necessary to form current, as (12) shows. If the four state variables

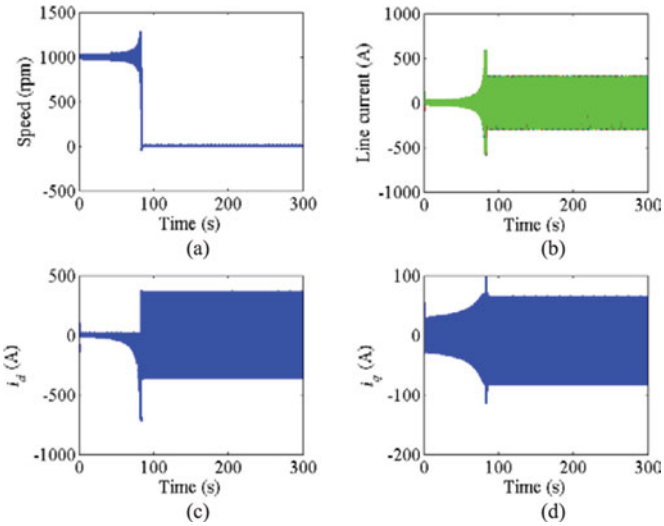

Fig. 4. Numerical calculation results for $t_f = 300$ ms. (a) Calculated mechanical velocity. (b) Calculated line currents. (c) Calculated d-axis current. (d) Calculated q-axis current.

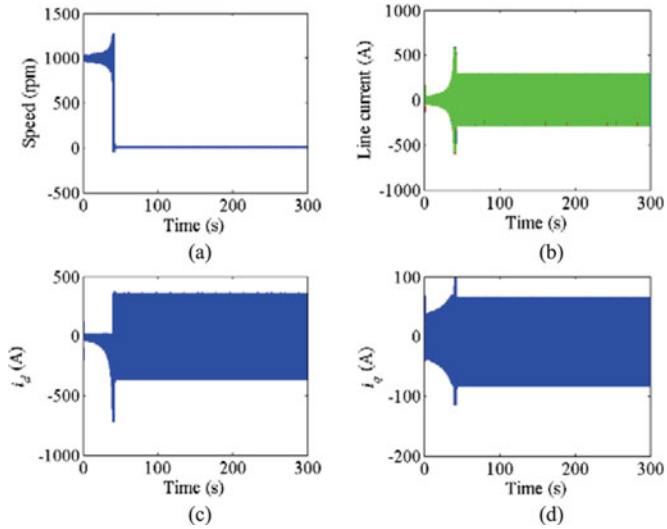

Fig. 5. Numerical calculation results when inverter voltage phase is 30° ahead of the grid at the time of switching. (a) Calculated mechanical velocity. (b) Calculated line currents. (c) Calculated d-axis current. (d) Calculated q-axis current.

in (12) can converge to stable values, the system is also stable. Basically, short switching time and proper parameter configurations are helpful for stability. Otherwise, if the switching dead time t_f is enlarged to 300 ms, the switching will fail as shown in Fig. 4. The mechanical speed diverges gradually and the prototype finally losses out of step. The phase current goes more than six times of the rated and the d-axis current oscillates with frequency of about 50 Hz, which may cause demagnetization and permanent damage to the machine.

Besides switching dead time, phase tracking between inverter and grid voltages is also crucial for safe switching, which is different from IMs and LSPMSMs. For IMs and LSPMSMs, phase tracking is not necessary because the rotor can be automatically dragged into synchronization with the help of rotor damping windings. However, for NLSPMSM, if the inverter voltage phase is not controlled close to the grid, for example with error of 30° ahead, the machine will lose out of step after switching, as shown in Fig. 5. During phase tracking, the fundamental magnitude of inverter output voltage should be close to that of grid so that the torque angles under inverter and grid drives are also close. Note that the inverter output fundamental voltage is mostly smaller than the grid; hence, there is an inevitable error in torque angle. The tiny error is acceptable for safe switching. However, when the inverter output voltage before switching is too small, the flux-strengthening current in d-axis will be needed.

Therefore, for a fixed NLSPMSM system, it is vital to minimize the switching dead time between contactor K1 and K2, and control the inverter output voltages in the same phase and magnitude as grid.

V. Control Strategy for Switching

To reduce the system cost, position sensorless control of NLSPMSM prototypes is adopted during inverter drive. Since motors are switched at their rated speed, the model-based method is adequate enough for position detection. Then, phase tracking between inverter and grid voltages is discussed and synchronous switching technic is implemented.

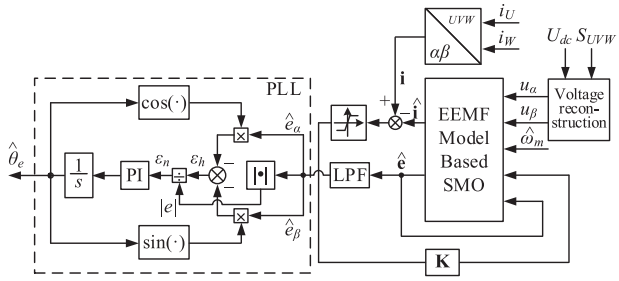

Fig. 6. Diagram for rotor position detection using EEMF model-based SMO.

A. Model-Based Position Sensorless Control

In this paper, SMO is designed based on the extended EMF (EEMF) model of IPMSM [29]–[31]. Both currents and EEMF are observed from SMO, and rotor position is obtained using PLL. The algorithm diagram is shown in Fig. 6, where the SMO is implemented as

$$\begin{bmatrix} \dot{\hat{\mathbf{i}}} \\ \dot{\hat{\mathbf{e}}} \end{bmatrix} = \begin{bmatrix} \hat{\mathbf{A}}_{\mathbf{11}} & \mathbf{A_{12}} \\ \mathbf{0} & \hat{\mathbf{A}}_{\mathbf{22}} \end{bmatrix} \cdot \begin{bmatrix} \hat{\mathbf{i}} \\ \hat{\mathbf{e}} \end{bmatrix} + \begin{bmatrix} \mathbf{B_1} \\ \mathbf{0} \end{bmatrix} \mathbf{u} + \mathbf{K} \cdot F(\mathbf{s}). \tag{20}$$

In (20), $\hat{\mathbf{i}} = \begin{bmatrix} \hat{i}_\alpha & \hat{i}_\beta \end{bmatrix}^{\mathrm{T}}$ and $\hat{\mathbf{e}} = \begin{bmatrix} \hat{e}_\alpha & \hat{e}_\beta \end{bmatrix}^{\mathrm{T}}$ are estimated currents and EEMF in stationary coordinate. $\mathbf{u} = [u_\alpha \; u_\beta]^{\mathrm{T}}$ is transformed from reconstructed voltages. $\mathbf{s} = [i_\alpha - \hat{i}_\alpha \; i_\beta - \hat{i}_\beta]^{\mathrm{T}}$. $\hat{\mathbf{A}}_{\mathbf{11}} = -\frac{R_1}{L_d} \cdot \mathbf{I} + \hat{\omega}_m \frac{L_d - L_q}{L_d} \cdot \mathbf{J}$, $\mathbf{A}_{12} = -\mathbf{B}_1 = -\frac{1}{L_d} \cdot \mathrm{I}$, and $\hat{\mathbf{A}}_{22} = \hat{\omega}_m \cdot \mathbf{J}$, where $\mathbf{I} = \begin{bmatrix} 1 & 0 \\ 0 & 1 \end{bmatrix}$ and $\mathbf{J} =$

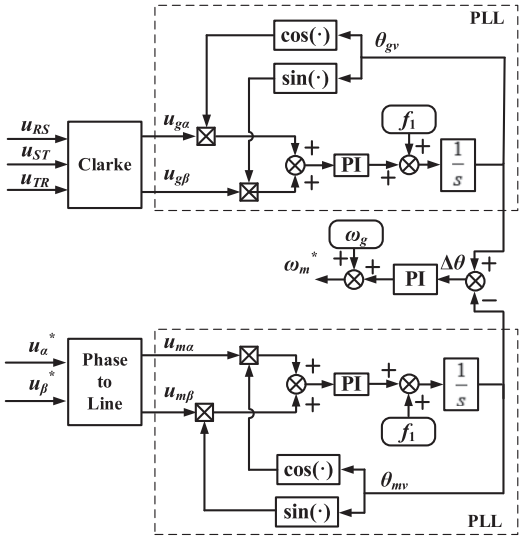

Fig. 7. Control diagram for phase tracking.

$\begin{bmatrix} 0 & -1 \\ 1 & 0 \end{bmatrix}$. **K** is the gain matrix of SMO. $F(\cdot)$ can be a saturation or sigmoid function.

B. Phase Tracking and Switching

It is the key principle to control inverter output voltages closed to grid voltages in frequency, magnitude, and phase for safe switching. The former two are much simpler because the mechanical velocity and space vector voltage can be precisely controlled close to the grid with proper velocity reference ω_m^* and *d*-axis current reference i_d^*. Therefore, only phase tracking is discussed. The phases of grid and inverter voltages are obtained from two PLLs as shown in Fig. 7, where frequency f_1 in PLL helps achieve faster regulation. Grid Clarke components $u_{g\alpha}$ and $u_{g\beta}$ are transformed from collected grid line voltages obtained from the voltage acquisition card. The output line voltages of general two-level three-phase voltage-source inverters lead phase voltages of $\pi/6$ with magnitude of $\sqrt{3}$ times. Therefore, the Clarke components of inverter line voltages $u_{m\alpha}$ and $u_{m\beta}$ are transferred from phase voltage references u_α^* and u_β^* for SVPWM as

$$\begin{bmatrix} u_{m\alpha} \\ u_{m\beta} \end{bmatrix} = \sqrt{3} \begin{bmatrix} \cos\frac{\pi}{6} & -\sin\frac{\pi}{6} \\ \sin\frac{\pi}{6} & \cos\frac{\pi}{6} \end{bmatrix} \begin{bmatrix} u_\alpha^* \\ u_\beta^* \end{bmatrix} = \frac{\sqrt{3}}{2} \begin{bmatrix} \sqrt{3}u_\alpha^* - u_\beta^* \\ u_\alpha^* + \sqrt{3}u_\beta^* \end{bmatrix}. \quad (21)$$

With proper designed PLL parameters, the phases of grid and inverter voltages, i.e., θ_{gv} and θ_{mv} can be obtained. The phase difference between θ_{gv} and θ_{mv} is treated as velocity adjustment of NLSPMSM for phase tracking. When the phase error $\Delta\theta$ is closed to zero, the switching condition is met and inverter outputs two digital signals for switching contactors. Note that contactor turn-on time is usually larger than turn-off time. Therefore, control signal for contactor K2 is generated no later than that for contactor K1 so that to minimize the switching dead time. After generating the two signals, inverter pulse width modulation (PWM) is disabled for safety.

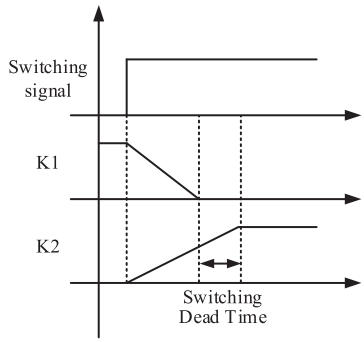

Fig. 8. Switching signal and actuation sequence of contactors.

C. Behavior of General AC Contactors

Numerical analysis has shown that the switching dead time between two contactors is significant for safe switching. However, general ac contactor used in this paper cannot response immediately to its control signal. When ac excitation signal is applied, it will take several times of collision for the contacts to finally close because of bouncing effect, and the power-on phase of ac voltage signal also affects the speed of contactor movable parts [32]. When excitation is cut off, for inductance load such as motor, the contactor cannot open immediately when there is working current. If the working current is very large, sharply cutting down the excitation signal will cause arc and further delay the open time. The detailed principle and modeling of ac contactors can be referred to [32]–[34]. In this paper, only the external characteristic of ac contactor, i.e., total switching dead time is concerned. For no-load switching when the working current is small, the contactor open time is usually shorter than close time. Therefore, the switching signals for the two contactors can be exerted simultaneously to get a short and safe switching dead time as shown in Fig. 8, especially for general ac contactor whose switching delay cannot be predicted exactly.

VI. Experimental Verifications

To sufficiently verify the aforementioned analysis and proposed control strategy, experiments are conducted on five NLSPMSM prototypes with different rated powers and velocities. The prototype parameters are listed in Table I, where the switching dead time t_f is obtained from tests. Note that the switching time varies with contactor capacity. Therefore, two sets of contactors with different rated currents are used to minimize the switching dead time, as shown in Fig. 9(b). The experiment platform is shown in Fig. 9(a), where two ARM-based inverters of 7.5 and 18.5 kW are used for soft start and switching control of different NLSPMSM prototypes and a 37 kW IM driven by ACS800 four-quadrant converter is used for load. A torque/speed sensor is mechanically connected between the prototype and IM, and the measured analog values (voltage output

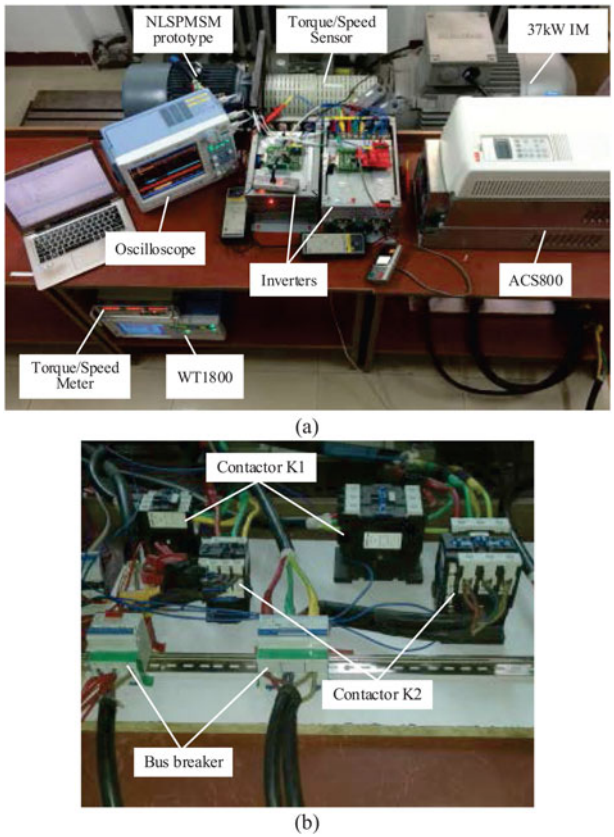

Fig. 9. Experiment platform. (a) NLSPMSM prototype and experiment devices. (b) Wiring configurations beneath the desk of ACS800.

for torque, pulse output for speed) are input to the WT1800 power analyzer so that the mechanical output power of the prototype can be measured. The grid input electrical power is measured using the voltage probes and current transformers. An ERN1387 encoder is mounted at the rear of IM, and the speed is tested using the other inverter. An oscilloscope is used to measure and record needed analog signals.

During test, the prototype is first driven to rated electric frequency of 50 Hz. Then, the phase tracking algorithm is applied, and the inverter output voltage is controlled in the same phase as grid voltage. Then, a switching signal is exerted and after a preset delay time, contactor K1 is open and contactor K2 is closed. Thus, the prototype is switched from inverter to grid drives, and efficiencies are tested with different loads exerted by ACS800 and IM.

Fig. 10 shows the inverter and grid voltages and their phase derivation after phase tracking adopting the control strategy proposed in Section V. It can be seen the inverter output voltage is controlled in the same phase as grid, which is qualified enough for switching.

Fig. 11(a) shows the whole soft start and synchronous switching procedure on the 37 kW NLSPMSM. The prototype is first driven to nominal velocity with the same frequency as grid, and the inverter voltage phase is adjusted to be the same as grid. When switching condition is met, contactor control signals are generated and the NLSPMSM is switched from inverter drive to

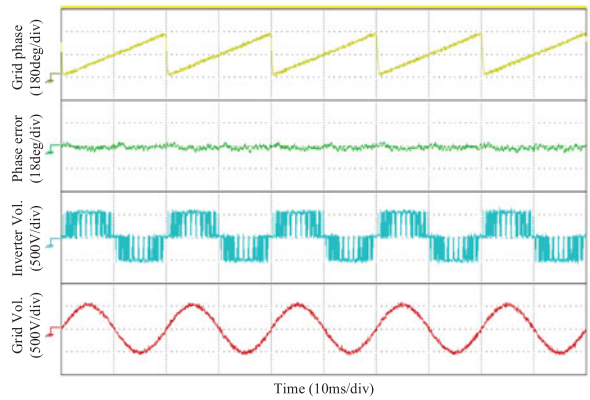

Fig. 10. Inverter and grid voltages after phase tracking.

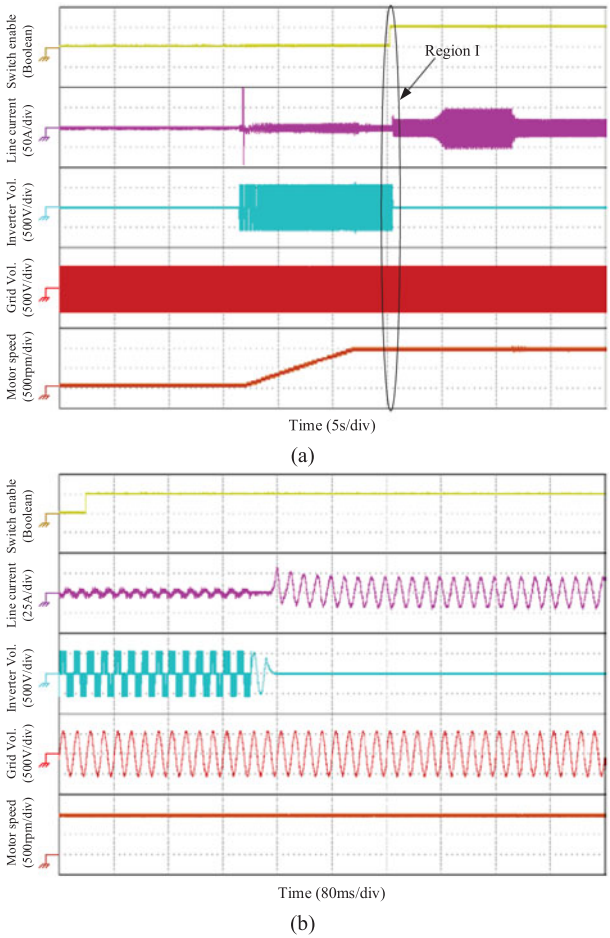

Fig. 11. Experimental waveforms of synchronous switching. (a) No load soft start, synchronous switching to grid drive and exerted step load. (b) Waveform expansion of Region I.

grid drive. Later on, 60% rated torque is loaded and unloaded, and the machine can still operate stably. The difference in line current amplitude before and after switching is because of the increase in supplied terminal voltage, which can be referred to Appendix I for detail. The voltage and current waveforms at the beginning of switching, i.e., region I in Fig. 11(a) are shown

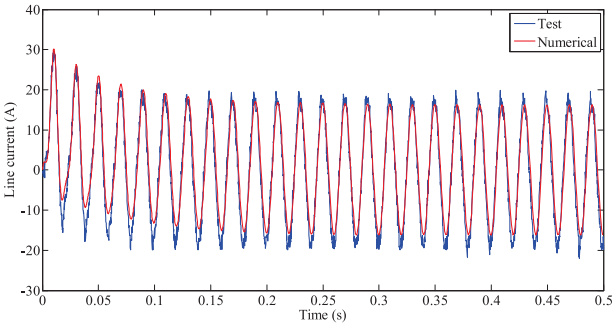

Fig. 12. Line current comparison between tested and numerical results for the first 0.5 s after contactor K2 is closed.

in Fig. 11(b). It can be seen the current stays zero for about 30 ms which is the switching dead time between two contactors. The inverter voltage waveform after PWM shutdown which is the back EMF of prototype is because of the turn-off delay of contactor K1. The tested current waveform is compared with numerical results obtained in Fig. 3(b) for the first 0.5 s after contactor K2 is closed, as shown in Fig. 12. It can be seen the numerical results is quite close to the tested, which testifies the derivations in Section III.

Synchronous switching to grid drive is also achieved on the other prototypes listed in Table I, and the switching waveforms are similar to that of the 37 kW prototype, as shown in Fig. 13, where all the prototypes are switched at light loads from inverter to grid drive, and then exerted rated torque. There is tiny difference caused by load shock, but the experiment procedure and achievement are the same. The system efficiencies under inverter and grid drives at rated velocities are then tested and compared, as shown in Fig. 14. The rated power of 37-kW prototype is not reached because the capacity of torque/speed meter is no more than 20 kW. It can be seen that inverter drive may be more efficient at light loads. However, when it comes to high loads, grid drive performs higher system efficiency considering the inverter loss, which is one of the major merits of grid drive.

Note that the inverter output apparent power during no-load soft start of the 37 kW NLSPMSM is only 1.57 kVA, which is quite small. Therefore, inverter with small capacity is enough for no-load switch so that to save the system cost. Generally, compared with 37 kW standard inverter, an 18.5 kW inverter is about 500$ cheaper, and another 500$ will be saved for a 7.5 kW inverter. Whereas the price of a voltage acquisition card is less than 20$, and that of two contactors with rated current of 80 A is around 100$. Therefore, the total extra hardware cost for the proposed method is no more than 120$. For the motor side, the thickness of PMs in LSPMSMs is usually more than twice larger than that of NLSPMSMs because of the large start current, which increases the assumption of PMs. Besides, the squirrel cages in LSPMSMs also increase the material and manufacture cost. Generally, the price of a 37 kW NLSPMSM is more than 1000$ cheaper than LSPMSM with the same rated power and speed. Based on the estimation, the system cost can be greatly reduced adopting the proposed solution.

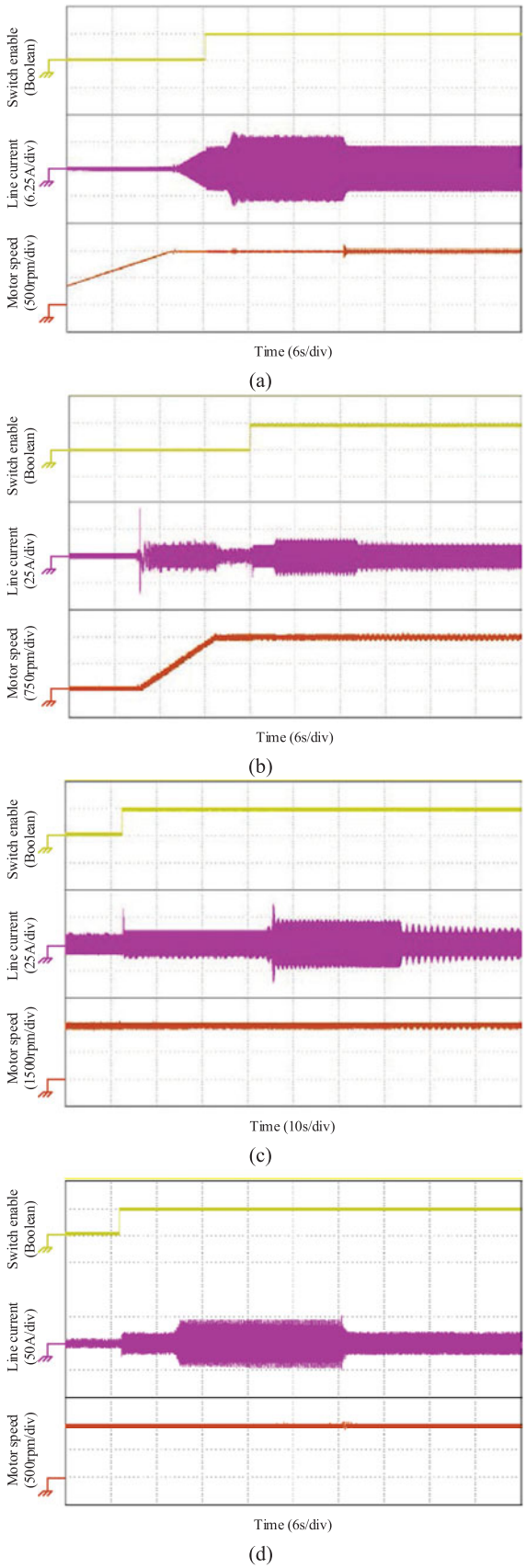

Fig. 13. Switching waveforms of the other prototypes. (a) 2.2 kW NLSPMSM, six poles. (b) 5.5 kW NLSPMSM, four poles. (c) 7.5 kW NLSPMSM, two poles. (d) 15 kW NLSPMSM, six poles.

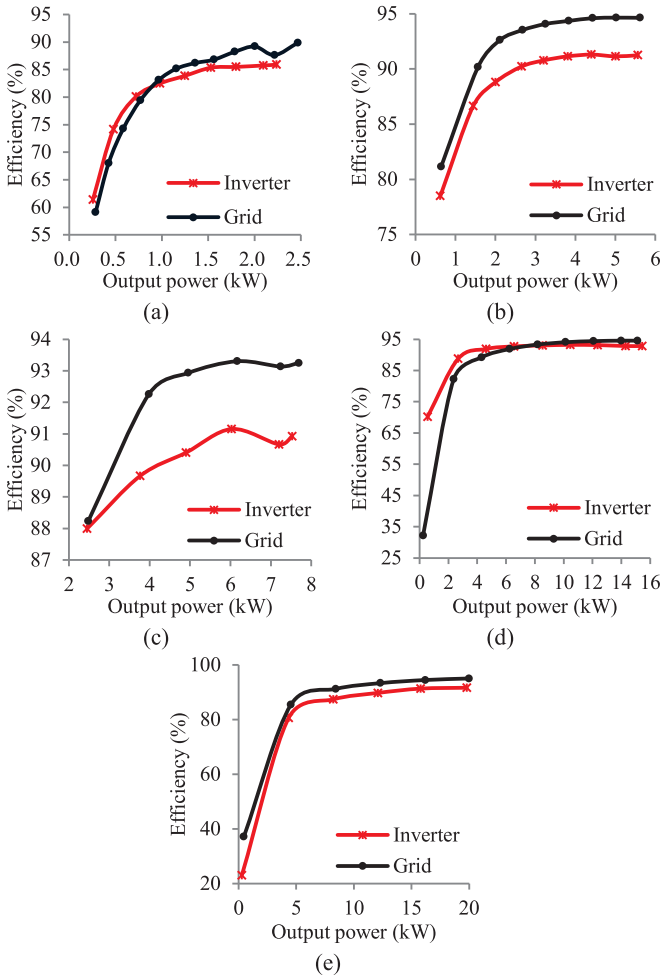

Fig. 14. System efficiency comparison between inverter drive at rated frequency and grid drive. (a) 2.2 kW NLSPMSM, six poles. (b) 5.5 kW NLSPMSM, four poles. (c) 7.5 kW NLSPMSM, two poles. (d) 15 kW NLSPMSM, six poles. (e) 37 kW NLSPMSM, six poles.

VII. Conclusion

The soft start and synchronous switching technic of NLSPMSMs from inverter to grid drives was originally proposed in this paper. The electromechanical state equations were deduced and the system stability was analyzed via numerical calculation, from which it was concluded the dead time between two contactors should be minimized as small as possible, and phase tracking was much more crucial for NLSPMSM than IMs and LSPMSMs for safe switching. The switching demands in voltage frequency, magnitude, and phase were met by adjusting the velocity and *d*-axis current references. To achieve the same phase between inverter and grid voltages, two PLLs were used to detect both phases and the same phase was achieved by regulating the phase error to zero. Experiments were done on five NLSPMSMs with different rated powers and velocities for vast verifications, and test results showed that all the machines were successfully switched to grid drive and robust to load variations. Efficiencies of the NLSPMSM system under inverter and grid drives were further compared, where the latter performed higher system efficiency especially at high loads.

Compared with IMs and LSPMSMs, NLSPMSMs have both high efficiency and excellent dynamic performance. With the feasibility driven by grid achieved in this paper, NLSPMSMs are promising for more applications so that to enhance the performance of electric drive systems, and more efficient control strategy can be expected when working at rated speed and high loads.

Appendix I

The electromagnetic torque T_{em} with respect to torque angle θ is known as

$$T_{em} = \frac{mpE_0U}{\omega_e^2 L_d}\sin\theta + \frac{mpU^2}{2\omega_e^2}\left(\frac{1}{L_q}-\frac{1}{L_d}\right)\sin 2\theta \quad \text{(A1)}$$

where m is the phase number, in this paper $m = 3$. E_0 is the RMS value of phase back EMF at electric velocity ω_e. U is the RMS value of phase terminal voltage. To simplify the following derivations, L_q is assumed equal to L_d, i.e., $L_q = L_d = L_s$. Then, the *d*- and *q*-axis currents at this torque angle is

$$\begin{cases} I_d = \dfrac{R_1 U\sin\theta + \omega_e L_s\left(E_0 - U\cos\theta\right)}{R_1^2 + \omega_e^2 L_s^2} \\ I_q = \dfrac{\omega_e L_s U\sin\theta - R_1\left(E_0 - U\cos\theta\right)}{R_1^2 + \omega_e^2 L_s^2} \end{cases} \quad \text{(A2)}$$

and the RMS value of phase current is

$$I_1 = \sqrt{I_d^2 + I_q^2} = \frac{\sqrt{E_0^2 + U^2 - 2E_0U\cos\theta}}{\sqrt{R_1^2 + \omega_e^2 L_s^2}}. \quad \text{(A3)}$$

From (A1)

$$\cos\theta = \sqrt{1 - \left(\frac{\omega_e^2 T_{em} L_s}{mpE_0U}\right)^2}. \quad \text{(A4)}$$

Substituting (A4) into (A3)

$$I_1 = \frac{\sqrt{E_0^2 + U^2 - 2\sqrt{E_0^2U^2 - \left(\frac{\omega_e^2 T_{em} L_s}{mp}\right)^2}}}{\sqrt{R_1^2 + \omega_e^2 L_s^2}}. \quad \text{(A5)}$$

The term $\omega_e^2 T_{em} L_s / mp$ is far less than E_0U during no-load switching, and (A5) can be approximated as

$$I_1 \approx \frac{|U - E_0|}{\sqrt{R_1^2 + \omega_e^2 L_s^2}}. \quad \text{(A6)}$$

It can be seen the phase current is mainly determined by the absolute difference between phase terminal voltage and back EMF. Before no-load switching, the RMS value of inverter output voltage is $U_{\text{inv}} = 363$ V which is measured from WT1800, and the RMS value of grid voltage is $U_{\text{grid}} = 380$ V. The tested RMS value of the 37 kW NLSPMSM prototype phase EMF at no load is 360 V. Therefore, the ratio of current amplitude under grid and inverter drive can be approximated as $|U_{\text{grid}} - E_0| / |U_{\text{inv}} - E_0| \approx 6.7$, and the tested ratio as shown in Fig. 11 is about 5.

REFERENCES

[1] P. E. Kakosimos, A. G. Sarigiannidis, M. E. Beniakar, A. G. Kladas, and C. Gerada, "Induction motors versus permanent-magnet actuators for aerospace applications," *IEEE Trans. Ind. Electron*., vol. 61, no. 8, pp. 4315–4325, Aug. 2014.

[2] A. Mahmoudi, S. Kahourzade, N. A. Rahim, W. P. Hew, and M. N. Uddin, "Design, analysis, and prototyping of a novel-structured solid-rotor-ringed line-start axial-flux permanent-magnet motor," *IEEE Trans. Ind. Electron*., vol. 61, no. 4, pp. 1722–1734, Apr. 2014.

[3] T. Marcic, B. Stumberger, and G. Stumberger, "Differential-evolution-based parameter identification of a line-start IPM synchronous motor," *IEEE Trans. Ind. Electron*., vol. 61, no. 11, pp. 5921–5929, Nov. 2014.

[4] M. A. Rahman, A. M. Osheiba, K. Kurihara, M. A. Jabbar, H. W. Ping, K. Wang, and H. M. Zubayer, "Advances on single-phase line-start high efficiency interior permanent magnet motors," *IEEE Trans. Ind. Electron*., vol. 59, no. 3, pp. 1333–1345, Mar. 2012.

[5] A. Hassanpour Isfahani and S. Vaez-Zadeh, "Line start permanent magnet synchronous motors: Challenges and opportunities," *Energy*, vol. 34, no. 11, pp. 1755–1763, 2009.

[6] J. Zhou and K. Tseng, "Performance analysis of single-phase line-start permanent-magnet synchronous motor," *IEEE Trans. Energy Convers*., vol. 17, no. 4, pp. 453–462, Dec. 2002.

[7] G. Feng, Q. Li, and B. Zhang, "Study on starting performance of a novel wound rotor line-start PMSM with WMW," presented at the International Conference on Electrical Machines and Systems, Beijing, China, 2011.

[8] P. Huang and M. Tsai, "Investigation of V-shaped line start permanent magnet motors based on reactance effect," *IEEE Trans. Magn*., vol. 49, no. 5, pp. 2311–2314, May 2013.

[9] J. Shen, P. Li, M. Jin, and G. Yang, "Investigation and countermeasures for demagnetization in line start permanent magnet synchronous motors," *IEEE Trans. Magn*., vol. 49, no. 7, pp. 4068–4071, Jul. 2013.

[10] A. D. Aliabad and M. Mirsalim, "Analytic modelling and dynamic analysis of pole-changing line-start permanent-magnet motors," *IET Electr. Power Appl*., vol. 6, no. 3, pp. 149–155, 2012.

[11] C. M. Stephens, G. B. Kliman, and J. Boyd, "A line-start permanent magnet motor with gentle starting behavior," in *Proc. IEEE 33rd IAS Annual Meeting*, St. Louis, MO, USA, 1998, pp. 371–379.

[12] E. Peralta-Sanchez, A. C. Smith, and J. J. Rodriguez-Rivas, "Steady-state analysis of a canned line-start PM motor," *IEEE Trans. Magn*., vol. 47, no. 10, pp. 4080–4083, Oct. 2011.

[13] F. Endrejat and P. Pillay, "The soft starters: Adjustable speed systems for multiple MW rated motors," *IEEE Ind. Appl. Mag*., vol. 14, no. 6, pp. 27–37, Nov./Dec. 2008.

[14] J. Nevelsteen and H. Aragon, "Starting of large motors—Methods and economics," *IEEE Trans. Ind. Appl*., vol. 25, no. 6, pp. 1012–1018, Nov./Dec. 1989.

[15] B. J. Chalmers, *Practical Electric Motor Handbook*. London, U.K.: Butterworths, 1988.

[16] K. Kurihara, T. Kubota, and M. Hori, "Steady-state and transient performance analysis for a single-phase capacitor-run permanent-magnet motor with skewed rotor slots," *IEEE Trans. Ind. Electron*., vol. 57, no. 1, pp. 44–51, Jan. 2010.

[17] E. C. Dos Santos, C. B. Jacobina, M. Beltrao De Rossiter Correa, and A. C. Oliveira, "Generalized topologies of multiple single-phase motor drives," *IEEE Trans. Energy Convers*., vol. 25, no. 1, pp. 90–99, Mar. 2010.

[18] F. J. T. E. Ferreira, M. V. Cistelecan, and A. T. De Almeida, "Comparison of different tapped windings for flux adjustment in induction motors," *IEEE Trans. Energy Convers*., vol. 29, no. 2, pp. 375–391, Jun. 2014.

[19] K. Sundareswaran and B. M. Jos, "Development and analysis of novel soft-starter/energy-saver topology for delta-connected induction motors," *IEE Proc. Electr. Power Appl.*, vol. 152, no. 4, pp. 922–932, 2005.

[20] X. Liang and O. Ilochonwu, "Induction motor starting in practical industrial applications," *IEEE Trans. Ind. Appl*., vol. 47, no. 1, pp. 271–280, Jan./Feb. 2011.

[21] C. Yeh and N. A. O. Demerdash, "Fault-tolerant soft starter control of induction motors with reduced transient torque pulsations," *IEEE Trans. Energy Convers*., vol. 24, no. 4, pp. 848–859, Dec. 2009.

[22] M. G. Solveson, B. Mirafzal, and N. A. O. Demerdash, "Soft-started induction motor modeling and heating issues for different starting profiles using a flux linkage ABC frame of reference," *IEEE Trans. Ind. Appl*., vol. 42, no. 4, pp. 973–982, Jul./Aug. 2006.

[23] A. Gastli and M. M. Ahmed, "ANN-based soft starting of voltage-controlled-fed IM drive system," *IEEE Trans. Energy Convers*., vol. 20, no. 3, pp. 497–503, Sep. 2005.

[24] G. Zenginobuz, I. Cadirci, M. Ermis, and C. Barlak, "Performance optimization of induction motors during voltage-controlled soft starting," *IEEE Trans. Energy Convers*., vol. 19, no. 2, pp. 278–288, Jun. 2004.

[25] V. V. Sastry, M. R. Prasad, and T. V. Sivakumar, "Optimal soft starting of voltage-controller-fed IM drive based on voltage across thyristor," *IEEE Trans. Power Electron*., vol. 12, no. 6, pp. 1041–1051, Nov. 1997.

[26] Z. Kaiqi, X. Dianguo, and W. Yi, "Discrete variable frequency soft starting on DSP-based voltage controller-fed IM drive," in *Proc. 29th Ann. Conf. IEEE Ind. Electron. Soc.*, Roanoke, VA, USA, 2003, pp. 758–763.

[27] G. Wang, R. Yang, and D. Xu, "DSP-based control of sensorless IPMSM drives for wide-speed-range operation," *IEEE Trans. Ind. Electron*., vol. 60, no. 2, pp. 720–727, Feb. 2013.

[28] G. Wang, H. Zhan, G. Zhang, X. Gui, and D. Xu, "Adaptive compensation method of position estimation harmonic error for EMF-based observer in sensorless IPMSM drives," *IEEE Trans. Power Electron*., vol. 29, no. 6, pp. 3055–3064, Jun. 2014.

[29] C. Zhiqian, M. Tomita, S. Doki, and S. Okuma, "An extended electromotive force model for sensorless control of interior permanent-magnet synchronous motors," *IEEE Trans. Ind. Electron*., vol. 50, no. 2, pp. 288–295, Apr. 2003.

[30] S. Sayeef, G. Foo, and M. F. Rahman, "Rotor position and speed estimation of a variable structure direct-torque-controlled IPM synchronous motor drive at very low speeds including standstill," *IEEE Trans. Ind. Electron*., vol. 57, no. 11, pp. 3715–3723, Nov. 2010.

[31] G. Wang, Z. Li, G. Zhang, Y. Yu, and D. Xu, "Quadrature PLL-based high-order sliding-mode observer for IPMSM sensorless control with online MTPA control strategy," *IEEE Trans. Energy Convers*., vol. 28, no. 1, pp. 214–224, Mar. 2013.

[32] M. Wada, H. Yoshimoto, and Y. Kitaide, "Dynamic analysis and simulation of electromagnetic contactors with AC solenoids," in *Proc. IEEE 28th Ann. Conf. Ind. Electron. Soc.*, 2002, pp. 2745–2751.

[33] J. Xiong, J. He, and C. Zang, "A dynamic model of electromagnetic relay including contact bounce," in *Proc. Int. Conf. Electr. Mach. Syst*., Wuhan, 2008, pp. 4144–4149.

[34] J. Riba Ruiz, A. Garcia Espinosa, and L. Romeral, "A computer model for teaching the dynamic behavior of AC contactors," *IEEE Trans. Educ*., vol. 53, no. 2, pp. 248–256, May 2010.

Ronggang Ni (S'14) received the B.S. and M.S. degrees in electrical engineering from the Harbin Institute of Technology, Harbin, China, in 2010 and 2012, respectively, where he is currently working toward the Ph.D. degree in power electronics and electrical drives in the School of Electrical Engineering and Automation.

His current research interests include efficiency-oriented design and control of electric machines, and system analysis of electric drives.

Dianguo Xu (M'97–SM'12) received the B.S. degree in control engineering from Harbin Engineering University, Harbin, China, in 1982, and the M.S. and Ph.D. degrees in electrical engineering from the Harbin Institute of Technology (HIT), Harbin, in 1984 and 1989, respectively.

In 1984, he joined the Department of Electrical Engineering, HIT, as an Assistant Professor, where he has been a Professor since 1994. He was the Dean of the School of Electrical Engineering and Automation, HIT, from 2000 to 2010. He is currently the Vice President of HIT. He has published more than 600 technical papers. His research interests include renewable energy generation technology, power quality mitigation, sensorless vector-controlled motor drives, high performance PMSM servo system.

Dr. Xu is an Associate Editor of the IEEE TRANSACTIONS ON INDUSTRIAL ELECTRONICS and the IEEE JOURNAL OF EMERGING AND SELECTED TOPICS IN POWER ELECTRONICS. He serves as Chairman of IEEE Harbin Section.

Gaolin Wang (M'13) received the B.S., M.S., and Ph.D. degrees in electrical engineering from the Harbin Institute of Technology, Harbin, China, in 2002, 2004, and 2008, respectively.

In 2009, he joined the Department of Electrical Engineering, Harbin Institute of Technology, as a Lecturer, where he has been a Professor of electrical engineering since 2014. From 2009 to 2012, he was a Postdoctoral Fellow in Shanghai STEP Electric Corporation. He has authored more than 30 technical papers published in journals and conference proceedings. He is the holder of seven Chinese patents. His current major research interests include permanent magnet synchronous motor drives, high performance direct-drive for traction system, position sensorless control of ac motors and efficiency optimization control of Interior PMSM.

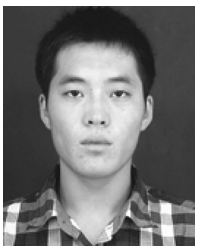

Guoqiang Zhang received the B.S. degree in electrical engineering from Harbin Engineering University, Harbin, China, in 2011, and the M.S. degree in electrical engineering from the Harbin Institute of Technology, Harbin, in 2013, where he is currently working toward the Ph.D. degree in power electronics and electrical drives in the School of Electrical Engineering and Automation.

His current research interest is in permanent magnet synchronous machine position sensorless control.

Chengrui Li received the B.S. degree in electrical engineering from the Harbin Institute of Technology, Harbin, China, in 2015, where he is currently working toward the Ph.D. degree in power electronics and electrical drives in the School of Electrical Engineering and Automation.

His current research interest is electric machine design.